CAMBRIDGE
UNIVERSITY PRESS

Forward ion acceleration by laser-driven collisionless filamentary shocks in underdense plasmas

P. Kordell[1], B. K. Russell[1,2], P. T. Campbell[1], K. Krushelnick[1,3] (ID),
A. Maksimchuk[1,2] and L. Willingale[1,2]

[1]The Center for Ultrafast Optical Science, University of Michigan, Ann Arbor, MI, USA; [2]Department of Electrical Engineering and Computer Science, University of Michigan, Ann Arbor, MI, USA and [3]Department of Nuclear Engineering and Radological Science, University of Michigan, Ann Arbor, MI, USA

Abstract

We have experimentally investigated the collisionless shock acceleration of ions via the interaction of a relativistic intensity (3×10^{19} W/cm^2), 1.053 μm wavelength laser pulse with an underdense plasma. This plasma is formed through the use of a novel cluster jet design that allows for control of the plasma peak density and front scale length without the use of additional plasma-forming laser pulses. When the front density scale length of the target plasma is less than 60 μm, the laser pulse (1 J, 400 fs) is capable of launching an electrostatic shock wave that accelerates a proton beam. This beam is shown to have a narrow divergence angle of 0.8°, a peak flux of 14×10^6 protons/sr with an ion energy exceeding 440 keV. Particle-in-cell simulations indicate this narrow ion beam is produced by converging shocks generated via filamentation of the laser pulse in high-density (near critical) plasma.

Introduction

The interaction of a relativistic intensity, short duration laser pulse with plasma has been shown to accelerate ions to energies on the order of the laser ponderomotive potential in underdense plasmas (Refs 1, 2) and 10 times the ponderomotive potential for overdense (Refs 3, 4) plasmas. Ions accelerated via 'Coulomb explosions' or the Target Normal Sheath Acceleration (TNSA) mechanism (Ref. 5) have garnered interest due to their applications which include high-energy density physics diagnostics (Ref. 6), and drivers for fast ignition fusion [Ref. 7, 8]. The extension of this ion source to applications such as hadron therapy or accelerator injection is difficult due to the need for narrow energy bandwidths. Experimental investigation of alternative laser-induced acceleration mechanisms including radiation pressure acceleration (9–11) and collisionless shock acceleration (CSA) (Refs 12–16) have shown promising beam characteristics with smaller energy bandwidths and narrow beam divergences.

In fact, CSA experiments using high-energy, short-pulse CO$_2$ laser drivers have produced particularly interesting results – generating proton beams having energy bandwidths of less than 10% and divergences on the order of 1°(Refs 12, 14). Successful acceleration of narrow bandwidth, multi-MeV ion beams via CSA has been performed experimentally via two techniques that are distinguished by the plasma density of the target, n_e. The first technique, referred to here as 'forward CSA', requires targets with peak densities in excess of the critical density $n_c = \varepsilon_o m_e \omega^2 / e^2$ at the frequency, ω of the driving laser pulse. As shown by Fiuza *et al.*, the ideal target for forward CSA uses a density profile with a steep linear ramp to the critical density followed by an exponential decay (Ref. 17). A laser interacting with the linear ramp will locally heat electrons at the critical density surface via the $\boldsymbol{J} \times \boldsymbol{B}$ mechanism or from the plasma waves produced by resonance absorption. These electrons can then expand into the target, pulling ions in the direction of the laser pulse and consequently steepening the ion density. The cumulative effect of electron heating and plasma density steepening forms an electrostatic shock wave that propagates into the downstream plasma. Sufficiently strong shocks can reflect downstream ions to twice the shock propagation velocity, resulting in an ion beam with a narrow energy bandwidth. A long plasma rear scale-length, much longer than the local Debye length, suppresses sheath fields that can distort the energy spectrum of accelerated ions. Several experiments have been conducted in the forward CSA regime using targets generated by gas jets steepened with multiple laser pulses (Ref. 12), ablated mylar targets (Ref. 13), pre-shocked or extremely high-pressure gas jets (Ref. 18).

The second technique (Ref. 16), referred to here as 'transverse CSA', involves focusing a single laser pulse with both high intensity and energy into an underdense plasma. Plasma-induced self-focusing of the pulse results in the ponderomotive heating of an electron column
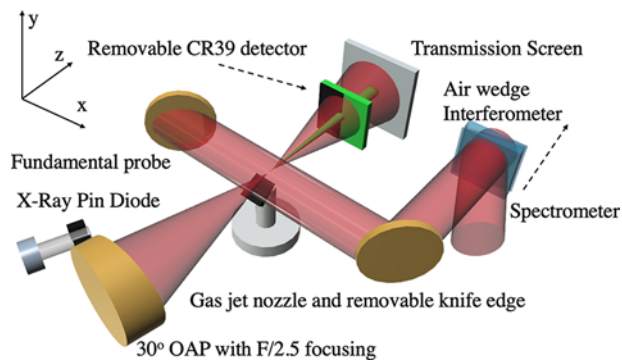
Figure 1. A schematic of the experimental setup used in this study.

which radially expands transversely from the direction of laser propagation into downstream plasma. The subsequent Coulomb explosion of ions forms a rapidly expanding plasma channel. If the expansion speed of the channel boundary is sufficiently large, channel ions overtake downstream ions. The resulting ion density pile-up can grow into a shock wave capable of downstream ion reflection. Transverse CSA results in a high divergence quasi-monoenergetic ion beam with a broad, radially expanding profile.

In this paper, we present measurements of a directional proton beam accelerated in the laser propagation direction via a third method; 'filamentary CSA' from the interaction of a single laser pulse with an underdense plasma just below the critical density. A profile similar to that proposed by Fiuza *et al.* is used for these experiments (Ref. 17). The short front plasma scale length enabled a tightly focused laser beam with modest energy and power to efficiently heat electrons via stimulated Raman scattering (SRS) (Ref. 19) and two Plasmon decay (TPD). However, particle-in-cell (PIC) simulations also reveal that extensive filamentation and hosing of the laser beam in the near-critical density plasma region results in the formation of multiple colliding transverse shockwaves which accelerate ions perpendicular to the collision direction with relatively narrow divergence. These shocks are produced in a multispecies (Ar/H) gas jet; therefore, this work is relevant to multispecies CSA – a research area with few published experimental (Ref. 13) or theoretical (Ref. 20) results.

Experimental setup

This experiment was conducted using the T-cubed (T^3) laser system at the University of Michigan. T^3 provides a single 8 J pulse with a 400 fs full-width-half-max (FWHM) pulse duration at a central wavelength of $\lambda = 1.053$ μm. The beam was focused onto the target with a $f/2$ off-axis parabolic mirror, as seen in Figure 1, to an asymmetric focal spot having a dimension of 7 μm by 4 μm. This focusing geometry resulted in vacuum intensities exceeding 3×10^{19} W/cm^2.

The laser pulse interacted with a gas/cluster target produced by a cylindrical, subsonic nozzle mounted to a solenoid valve. The valve was cooled with a liquid nitrogen-filled copper jacket capable of maintaining a minimum temperature of 160 K. Higher temperatures were stabilized by a mica-insulated band heater.

The valve was backed with an argon–hydrogen mixture (97% Ar, 3% H) which provided a high electron density gas was released

through a nozzle with an inner diameter of 300 μm which was positioned a distance of 300 μm below the laser focus. The backing pressure could be varied up to about 9 MPa.

A 3% pellicle reflection of the main pulse was used to probe the interaction orthogonal to the propagation direction of main beam. This probe was imaged by an interferometer with a resolution of 60 μm which measured the plasma density scale lengths in different target arrangements and for different backing gas temperatures and densities. The spatial resolution was limited by the experimental geometry and the quality of the probe beam reflected from the pellicle. Imaging a near-critical density plasma with a fundamental frequency probe is not possible due to the combination of scattered light at the fundamental and plasma refraction effects, so the images seen in Figure 2 were taken with the laser power attenuated by a factor of 10 and reduced backing pressure (0.3 MPa for plain nozzle and 1.6 MPa for knife-edge).

At a 300 μm standoff distance, the interaction of the laser with the plain nozzle target produced a plasma that had a density scale length of 300 μm (see Figure 2A). Shorter scale lengths were obtained by placing a knife-edge above the nozzle orifice. High-pressure gas motion around the edge created a supersonic shock wave which resulted in plasma with a laser facing (front) scale length of 80 μm (Figure 2B). Further reduction of the front scale length was available in this arrangement via clustering. Cooling of the backing gas to near the thermodynamic critical temperature combined with adiabatic cooling via subsonic expansion produced a clustered media target (Ref. 21) as close as 400 μm above the nozzle orifice.

At this height, the knife-edge produced a front density scale length less than 60 μm (the resolution limit of the interferometer), while preserving a longer scale length at the target rear required to suppress sheath fields (see Figure 2). The Hagena parameter (Ref. 22), a dimensionless quantity that describes clustering behaviour, scales favourably with pressure. Therefore, target scale lengths should be further reduced at higher backing pressures. The peak density at full beam power and higher backing pressure was calculated in two steps. A linear increase in the number density of the backing gas due to the higher pressure was calculated, and then the increase in the degree of ionization of the target gas due to the higher laser power was scaled according to field ionization estimates. The error involved in these assumptions is responsible for the relatively large electron density error bars shown in Figure 4. A nuclear track detector, allyl-diglycol carbonate (CR39), was positioned in the forward direction to detect accelerated protons. A 4 μm layer of aluminized mylar shielded the CR39 from exposure to the intense laser light present in these experiments. Half of the CR39 piece was shielded with 3 mm of aluminium to provide a background measurement. Microscopic images of the CR39 were registered together with the ImageJ Stitching Toolbox (Ref. 23). Tracks in the registered images were located with a custom computer vision code and were used to make a map of CR39 signal. This code was found to count tracks with an error of 5% when compared to manual counting.

The interaction of the laser with plasma electrons was monitored with three diagnostics. keV x-ray emission from the plasma was monitored using an x-ray PIN diode having a dipole magnet in front of it to reduce signals from charged particles. The transmission of light through the target was measured with a scattering screen positioned behind the gas jet that was imaged through a 10 nm FWHM fundamental bandpass filter centred at $\lambda = 1.053$ μm. Unfiltered, side scattered light was collected and imaged with the optics of the probe system as previously described.
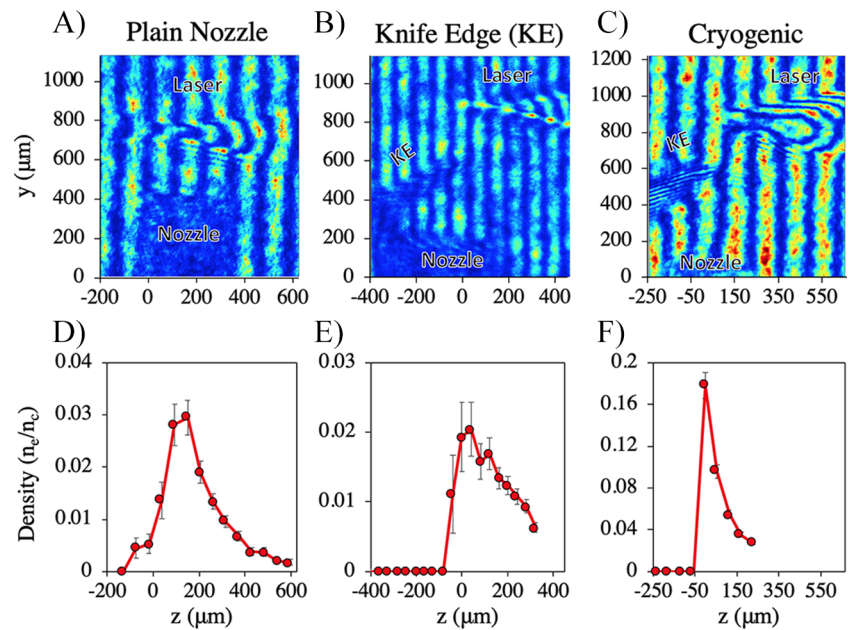
Figure 2. Interferometric images of the plasma density profiles from different target arrangements taken at low laser power and backing pressure. The nozzle appears as a shadow in the lower portion of the images while the laser propagates from the right to a focus at $z = 0$ µm. The top row shows raw interferograms while the bottom row shows electron density lineouts along the laser axis. (A, D) show the plain nozzle arrangement with the longest plasma density scale lengths of 300 µm. (B, E) show the moderate front scale length of 80 µm from the knife-edge arrangement with room temperature backing gas. (C, F) show the shortest scale length plasma of <60 µm (beyond imaging resolution). This plasma was produced when the target was both in the knife-edge arrangement and backed with cooled gas. The backing pressure was 0.3 M MPa for plain nozzle and 1.6 MPa for knife-edge.

Table 1. Summary of target conditions and corresponding proton signal for data as shown in Figure 3

Arrangement	Plain Nozzle	Knife-Edge
Backing pressure (MPa)	2.1	8.3
Backing Temp. (K)	296	165
Front scale length (µm)	~ 300 (Long)	< 60 (Short)
Backing gas	CH_4	97%Ar/3%H
Peak n_e (n_c)	0.21 ± 0.03	0.95 ± 0.15
Shots accumulated	2	4
Mean p^+ flux (N/sr)	1.7 ± 0.2 × 10^5	7.0 ± 0.1 × 10^5
p^+ energy range (keV)	880 < E < 1060	440 < E
r beam div (mrad)	168 ± 19	18 ± 1.7
x pointing (mrad)	12 ± 5	19 ± 5
y pointing (mrad)	−31 ± 5	−73 ± 5

Additionally, the side scattered light was spectrally characterized with an optical/infrared spectrometer.

Results

Protons accelerated from the interaction of the laser pulse with the target were observed with the target in both the plain nozzle and knife-edge target arrangements.

The plain nozzle arrangement produced signal with the long scale lengths shown in Figure 2A, d and a relatively low peak electron density of $0.21n_c$ – $0.03n_c$. The knife-edge arrangement produced protons with the short scale length <60 µm seen in Figure 2C, f with a higher peak plasma density of $0.95\ n_c$ – 0.15 n_c. Table 1 contains further details on the plasma conditions and resultant proton signal.

Histograms of the spatial distribution of signal on the CR39 are shown in Figure 3. Figure 3A shows the accumulated signal from two shots taken with the plain nozzle arrangement and Figure 3B shows signal from 4 shots in the knife-edge arrangement.

Forward accelerated protons from plasmas with different scale lengths and peak densities showed differing properties. Protons from plasma with a peak density of 0.2 n_c and long scale lengths (300 µm) with a kinetic energy, E, satisfying 1 MeV > E > 880 keV had an average signal of 1.7×10^6 protons/sr. This beam had a relatively large total angular divergence of 168 mrad. Ion beams with angular divergences of approximately 100 mrad have previously been measured from very underdense gas targets and the acceleration mechanism was attributed to TNSA (Ref. 24). Protons from the plasma with a high peak density (0.95 n_c) and a short front scale length (<60 µm) accelerated a larger proton flux of 7.0×10^6 protons/sr with E > 440 keV. This represents a 17-fold increase in observed signal per shot compared to the lower density plasma. This flux increase is more dramatic when the difference in proton density between a 97%Ar /3%H and CH_4 is taken into account. At peak intensity, the T^3 laser is capable of ionizing argon to Ar^{14+} through barrier suppression ionization. Even higher states of ionization may occur due to collisional processes. The argon/hydrogen mixture will give a ratio of proton to electron density within the plasma of $p^+/e^- = 3/(97 \times 14 + 3) = 0.2\%$. CH_4 has a much higher p^+/e^- ratio of 40%. Therefore, the short scale length, high-density plasma created from our cryogenic knife-edge target arrangement accelerated about three orders of magnitude more protons per plasma electron than a plain nozzle target. Protons generated from the near-critical target also have a much smaller angular divergence of 14 mrad. CSA experiments on both 10 and 1 µm wavelength laser systems have produced beams with divergences of 26 and 12 mrad, respectively (Refs 12, 18). This experimentally measured narrow proton beam divergence suggests CSA is the acceleration mechanism from our high-density, short-scale plasma.

For information about the laser−plasma interaction that produces these proton beams, we consider the x-ray emission and laser energy transmission signals as a function of the peak plasma density. Measurements from the plain nozzle arrangement are shown in Figure 4A, B. As the peak electron density increases, the transmission decreases to a minimum of 10% at a density of 0.3 n_c.
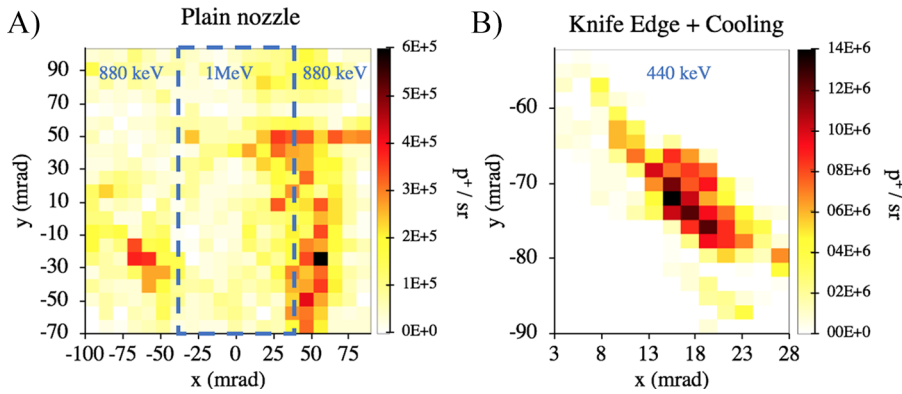
Figure 3. A map of the spatial distribution of proton flux on the CR39 detectors produced from counting ion tracks The centre of the laser vacuum propagation axis is through $x = 0$ mrad and $y = 0$ mrad. (A) shows the signal from a low density (0.2 n_c), long scale length (300 μm) plasma. Signal contained within the dashed box corresponds to proton flux with an energy exceeding 1 MeV while signal outside the box is from proton flux exceeding 880 keV. (B) shows the signal from a high density (0.95 n_c), short front scale length (<60 μm) plasma. Protons within this region of the detector have energies exceeding 440 keV. The different energy ranges are produced through use of different filter thicknesses.
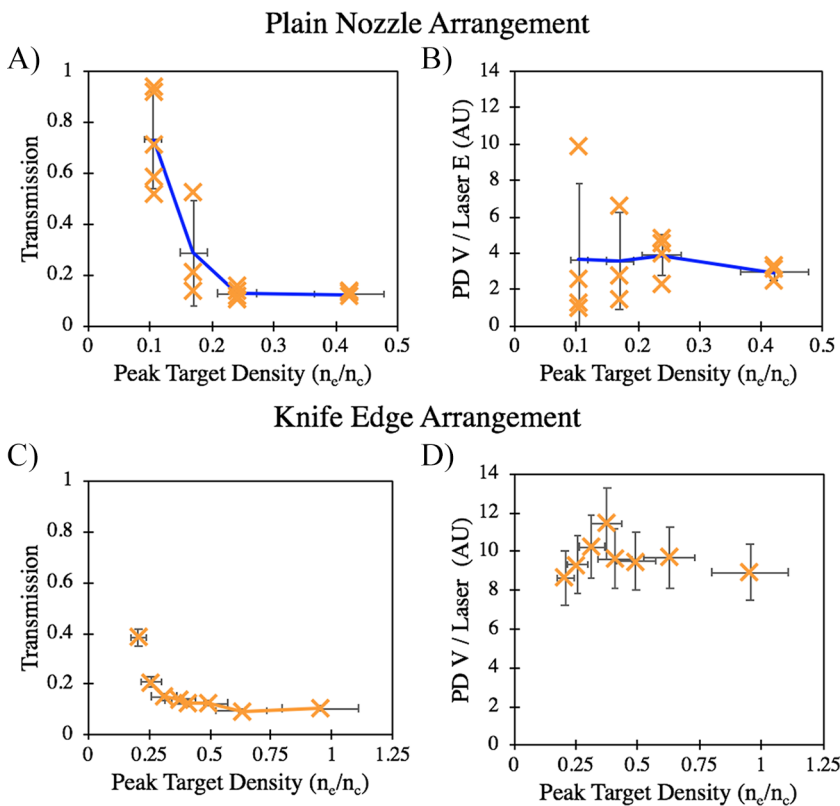

Figure 4. (A) Shows the laser light transmission and (B) the x-ray signal normalized to laser energy for the plain nozzle configuration with varying peak density. (C, D) show the same quantities for the knife-edge arrangement. Error bars show the standard shot to shot deviation in the measurement.

Therefore, it is likely that a considerable fraction of electron heating and laser energy deposition occurs via plasma wave generation from SRS and/or TPD of which both occur at or below 0.25 n_c ('quarter critical'). These instabilities transfer incident laser energy into scattered radiation and high phase velocity plasma waves which subsequently heat the plasma through collisional damping. The transmitted laser light and x-ray signal (indicative of electron heating) vary significantly shot to shot within this density range as expected if the heating mechanism is largely due to laser plasma instabilities. The T³ FWHM pulse duration, $\tau = 400$ fs, has a pulse length of $l = c\tau = 120$ μm, which is less than the 300 μm density scale length of the target. This condition means the SRS and related 'self-modulation' instability is likely a major cause for the fluctuations in the interaction observed in our diagnostics.

Measurements from the knife-edge arrangement (<60 μm scale length) are shown in Figure 4C and 4D. With a shorter scale length, our laser pulse length, $l = c\tau$, was half of the plasma scale length. This limited the growth of the SRS/TPD and self-modulation instabilities, resulting in a more stable electron heating and laser transmission throughout our tested peak density range. The x-ray signal remained relatively stable over all densities and was on average equal to the very largest signals observed from our plain nozzle arrangement. Denser targets yet again corresponded to a reduced laser transmission that reaches a minimum of 15% for peak electron densities above 0.3 n_c. This suggests that despite the presence of a much shorter scalelength and a near-critical peak density, the laser still coupled mostly to the underdense plasma.

Images of the side scattered light from shots taken with the knife-edge arrangement showed strong scattering from the plasma both in front of and behind the peak density region. Side scatter from the shots that produced the narrow divergence proton signal in Figure 3B are shown in Figure 5. This shows the degree of
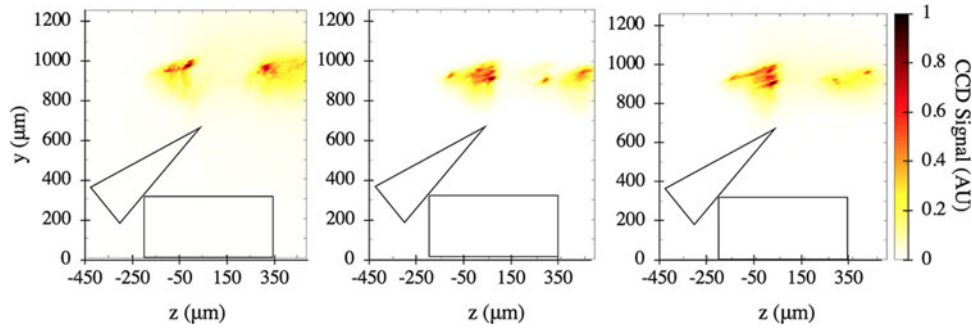
Figure 5. Images of side scattered light from three different full power shots (laser propagates left to right) on a clustered target during exposure of the CR39 shown in Figure 3. The positions of the nozzle and knife-edge are drawn in black while the laser is focused at $z = 0$ μm. Side scatter occurs dominantly at the target front. Differences observed are indicative of shot-to-shot fluctuations in the interaction.
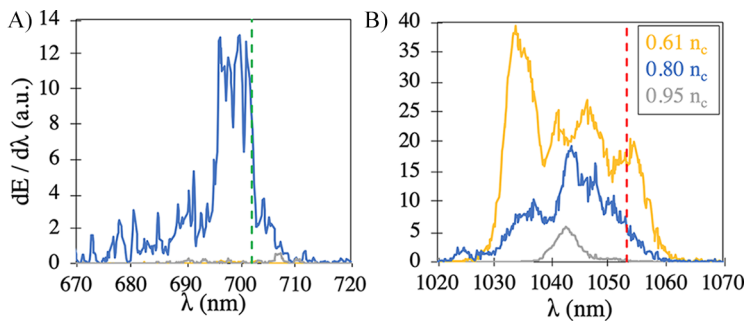

Figure 6. Spectrum of side scatter observed with the knife-edge configuration. Three shots with different backing conditions are shown. Signal distributed about the 3/2 harmonic (702 nm, dashed green line) is shown in (A) while signal distributed about the fundamental (1053 nm, red dashed line) is shown in (B).

experimental fluctuations in the data. Scattered light originated from two specific regions of the plasma. The first was positioned 50 μm in front of the location of the peak target density while the second was 150 μm behind the laser focus.

Spectral measurements of this side scattered light corroborate the evidence from the transmission measurements that the laser is scattering from plasma waves generated during the interaction. Figure 6 shows that scattered light is spectrally distributed around both the fundamental and 3/2 harmonic of the laser frequency. Both spectral components exhibit blue shifting, broadening and modulation. Side scattered fundamental light may be the result of several processes including Thomson Scattering, Brillouin Scattering or Mie scattering from the gas clusters. Given the large density transitions present in the plasma, ionization induced blue-shifting (Ref. 25) is likely responsible for the modification of the fundamental spectrum. 3/2 Harmonic light is indicative of TPD near quarter critical density which supports the evidence from the transmission and x-ray diagnostics that a subcritical heating mechanism is primarily responsible for hot electron generation. In linear theory, the growth rate of TPD (Ref. 26) increases linearly with laser electric field (Ref. 27) and SRS (Ref. 28) increases linearly with both the laserelectric field and the plasma electron density (Ref. 19). Therefore we expect that these processes will have a much greater effect on CSA experiments conducted with higher intensity 1 μm lasers than with 10.6 μm CO_2 systems having similar pulse durations.

Simulations

To investigate the mechanism by which ions could be accelerated in this regime, two-dimensional (2D) PIC simulations were performed using the code OSIRIS with realistic experimental conditions (Ref. 29). A 1200×720 (c/ω_{pe}) box was used with a grid of 3600×2160 cells and 64 particles per cell for each particle species. The box was filled with three particle species, electrons, protons and Ar^{14+}, all using the density profile along the x-direction from Figure 2F for a cooled gas jet with a knife-edge. This density profile was scaled based on maximum electron densities ranging from 0.1 to 1.1 n_c. The density profile was tapered to zero near the walls in the y-direction to reduce boundary effects. The relative density of ion species was calculated based on the 97%Ar/3%H gas mixture with protons and Ar^{14+} making up approximately 0.2% and 99.8% of the positive charge density respectively. Absorbing boundary conditions were used for particles on all boundaries, and open boundary conditions were used for the electro-magnetic fields. A 716 $1/\omega_0$ FWHM laser pulse was injected from $x = 0$ and focused with an $a_0 = 4.87$ at various positions in x with a FHWM spot size of 41.77 c/ω_0, where ω_0 is the laser frequency. Figure 7 shows the propagation of a laser pulse focused at the peak of the density gradient ($x = 360$ c/ω_0) and polarized in the x-y plane. Simulations were performed with peak electron densities of 0.1 n_c (row 1), 0.95 n_c (row 2) and 1.1 n_c (row 3). Row 1 shows highly underdense propagation where the laser pulse rapidly generates a channel without significant filamentation, and shocks that are purely transverse to the laser propagation direction are formed. This was previously shown by Wei et al. (Ref. 16).

In the higher density cases shown in rows 2 and 3, transverse shocks are still formed in both ion species, but the laser does not reach the +x-boundary due to filamentation and scattering. In both high density cases a forward propagating shock is not seen to form as a result of density steepening at the front of the laser, but instead forward propagating shocks form due to hosing and filamentation of the laser, turning transverse shocks into longitudinal shocks. In row 3, transverse shocks from two large filaments are
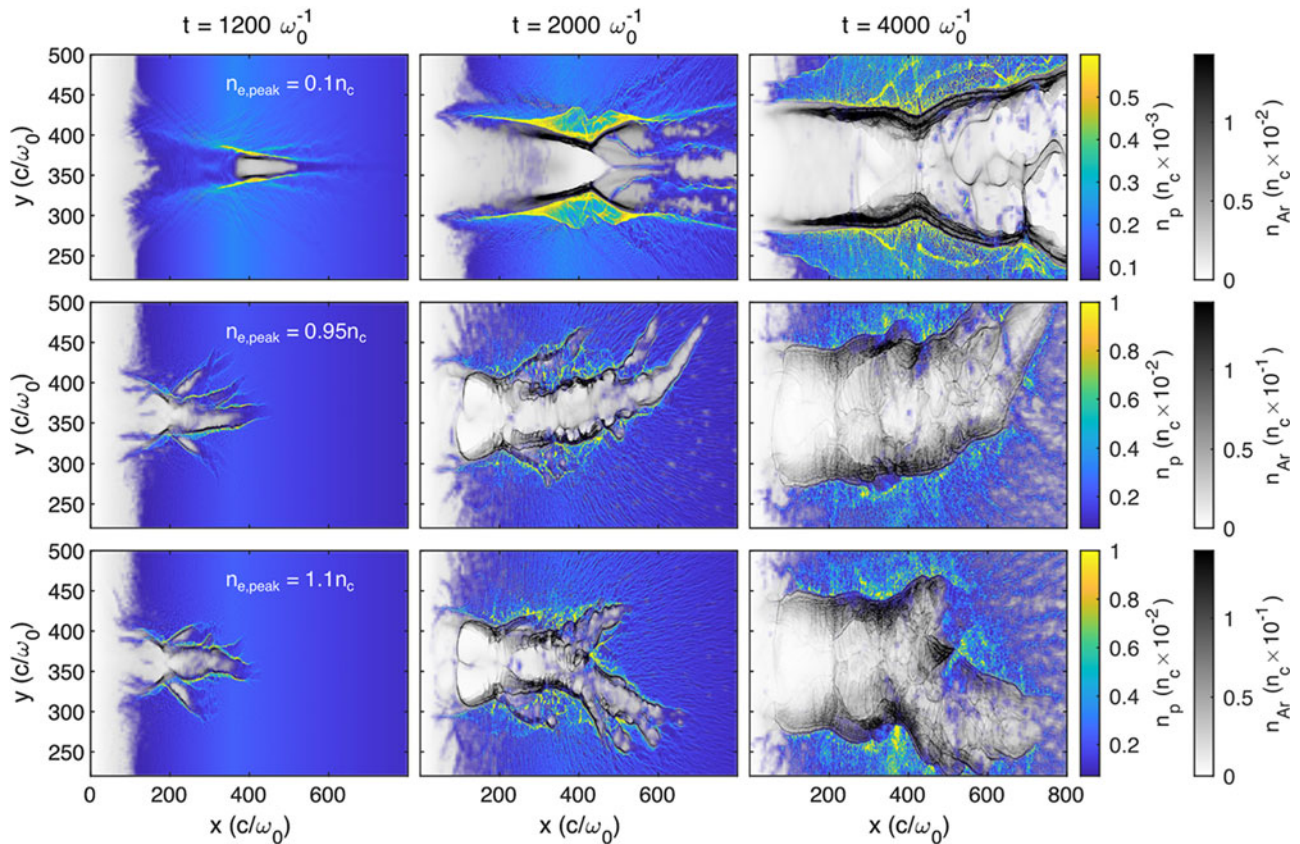
Figure 7. Propagation of a realistic T-cubed laser pulse through the density profile shown in Figure 2C made up of H^+ and Ar^{14+} with peak densities of 0.1 n_c (row 1), 0.95 n_c (row 2) and 1.1 n_c (row 3).

seen to converge, confining the protons and accelerating them in the positive x-direction. The convergence angle of these two filaments is much too large to generate the small diverge seen in experiment (Figure 3). This beam is better explained by the small filaments that split from the main channel seen in row 2 of Figure 7. These filaments break from the channel at small angles and would only confine the beam in one direction, generating an elongated spot as was seen in experiment. The elongated spot observed from the 2D data could also be due to effective 'hosing' of the proton beam through the plasma in three dimensions.

As was previously noted, using the experimentally measured density profile we were unable to drive a forward-propagating shock from density steepening at the front of the laser pulse. A possible explanation could be that the size of the focal spot was too small compared to the expansion of the plasma; therefore, the plasma escaped the region of the shock before reflection, as noted by (Ref. 17). To test this, the focal spot was increased at the position of peak density by focusing the laser further into the density down-ramp. This is a realistic case because the nozzle was scanned along the laser propagation direction within the range of a few hundred micrometres to optimize the x-ray signal during the experiment. We performed simulations using a peak density of 1.1 n_c and 0.95 n_c with different focusing positions. Even with a larger focal spot, within the range of possible realistic experimental parameters, we were unable to drive purely forward propagating shocks.

To better understand how protons interact with converging shocks, particle tracking was performed. Using the density and phase space shown in Figure 8A and B, 100 protons with momenta

exceeding 0.055 $m_p c$ and positions between the converging shocks were tracked. Figure 8C shows the paths of four protons overlaid on the Ar^{14+} ion density in the rectangular region marked by a white, dashed rectangle in (A). The colour of the proton paths represents the energy of each particle. In the population of 100 accelerated protons, many trajectories were observed with particles experiencing single or multiple reflections. The particles which only experienced a single reflection were able to do so because there were reflected from one of the shocks at a small angle to the x-axis, thereby allowing them to escape the region between the converging shocks without experiencing any subsequent reflections. The paths which are plotted in Figure 8C are those of particles which experienced multiple reflections. These reflections can be seen as abrupt changes in the particle direction and energy. To experience multiple reflections, the particles must meet two conditions. Firstly, the trajectory of the particle after reflection from the first shock must intersect the second shock. Secondly, the kinetic energy of the particle normal to the second shock, in the frame of the second shock, cannot exceed the potential energy of the shock. If this condition is not met, the particle will move through the shock and will not be confined. By also noting that the particle will obtain an increased velocity in the normal direction of the shock at each reflection, we can see that there must exist an optimal angle between the converging shocks where a particle reflected from one shock will experience the largest number of reflections, and thereby gain the largest energy in the forward (x) direction without passing through a shock. We can also note that the divergence angle of the confined proton beam will be approximately the same as the angle between
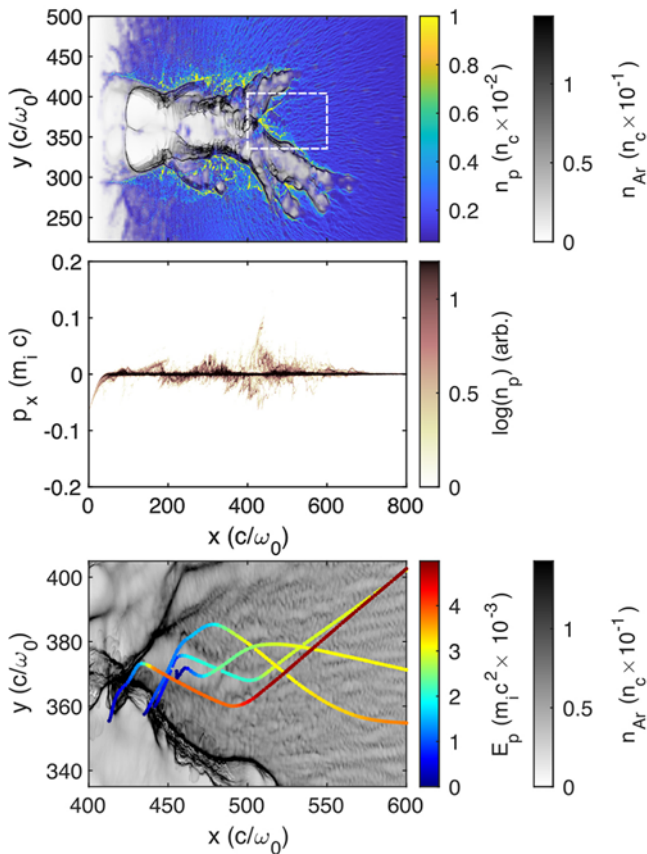
Figure 8. Simulation of the propagation of a laser pulse into a plasma density profile having a peak density of 1.1 n_c at a time: $t = 2000\ 1/\omega_0$. (A) Transverse shocks from filaments focus and accelerate protons as seen in (B) which shows a sharp jump in proton momenta. Particle tracking in (C) shows a random selection of accelerated protons experiencing multiple reflections from interactions with the shock structures.

the shocks, although this is not always true. The shocks are generally not planar in shape, and can instead have curved structures which will greatly change the confinement and reflection angles.

From Figure 3B, this suggests that the small divergence beam of protons was generated by a set of filaments that generated shocks which converged with an angle of ∼20 mrad assuming the filaments had a simple linear structure. Due to the stochastic nature of filamentation, it is possible that two filaments could be created with this angle, or that a filament could split from the main channel with this angle. With the angle being small it is also likely that these protons would experience multiple reflections, therefore reaching an energy >440 keV as was seen in experiment is very reasonable, based on the much higher energies of 1 MeV seen after a single reflection in simulation. The experimental data also showed that the proton bunch was found several milliradians from the laser axis and had a line-like shape which is consistent with this acceleration mechanism. A filamentary proton beam could also produce a '2D' elongated structure as seen in the experimental data. If a larger detector was used, one would expect that several bunches of these protons could be found scattered across the detector. This acceleration mechanism may also explain the experimental results reported by Puyuelo-Valdes *et al.* where the interaction of a laser with a relativistically underdense gas jet generated high-energy protons at several different angles that changed from shot-to-shot (Ref. 30).

Clearly, more accurate simulations describing the detailed physics should be performed in 3D in the future; however, due to the expense of 3D PIC simulations running for picosecond durations, they were not performed for the present work.

Conclusion

We have presented measurements of forward accelerated, narrow divergence proton beams produced by the interaction of a relativistic laser pulse with an underdense plasma. The beam flux of the CSA ion beam was found to accelerate three orders of magnitude more protons per plasma electron than the TNSA mechanism from the same laser. We note that despite this large increase in signal, total ion flux is still below TNSA from solid targets. PIC simulations show that these ions are accelerated by converging shocks generated by laser filamentation. These filaments can stochastically produce very narrow divergence beams as they confine the beam in a single transverse direction during acceleration. Acceleration by transverse converging shocks could be controlled using two laser pulses propagating through a low-density gas jet at a set angle, or by using a laser pulse with a Laguerre–Gaussian mode beam profile, potentially allowing for radial confinement of a shock accelerated beam. This study of CSA with 1 μm wavelength, single pulse laser with relatively low power (∼15 TW) was enabled by our cryogenic target design, the first such used in CSA experiments.

References

1. Krushelnick K, Clark EL, Najmudin Z, Salvati M, Santala MIK, Tatarakis M, Dangor AE, Malka V, Neely D, Allott R and Danson C (1999) Multi-MeV ion production from high-intensity laser interactions with underdense plasmas. *Physical Review Letters* **83**, 737. doi:10.1103/PhysRevLett.83.737

2. Sarkisov GS, Bychenkov VY, Novikov VN, Tikhonchuk VT, Maksimchuk A, Chen SY, Wagner R, Mourou G and Umstadter D (1999) Self-focusing, channel formation, and high-energy ion generation in interaction of an intense short laser pulse with a He jet. *Physical Review E* **59**, 7042. doi:10.1103/physreve.59.7042

3. Clark EL, Krushelnick K, Davies JR, Zepf M, Tatarakis M, Beg FN, Machacek A, Norreys PA, Santala MIK, Watts II and Dangor AE (2000) Measurements of energetic proton transport through magnetized plasma from intense laser interactions with solids. *Physical Review Letters* **84**, 670. doi:10.1103/PhysRevLett.84.670

4. Maksimchuk A, Gu S, Flippo K, Umstadter D and Bychenkov VY (2000) Forward ion acceleration in thin films driven by a high-intensity laser. *Physical Review Letters* **84**, 4108. doi:10.1103/PhysRevLett.84.4108

5. Snavely RA, Key MH, Hatchett SP, Cowan TE, Roth M, Phillips TW, Stoyer MA, Henry EA, Sangster TC, Singh MS, Wilks SC, MacKinnon A, Offenberger AA, Pennington DM, Yasuike K, Langdon AB, Lasinski BF, Johnson J, Perry MD and Campbell EM (2000) Intense high-energy proton beams from petawatt-laser irradiation of solids. *Physical Review Letters* **85**, 2945. doi:10.1103/PhysRevLett.85.2945

6. Borghesi M, Campbell DH, Schiavi A, Haines MG, Willi O, MacKinnon AJ, Patel P, Gizzi LA, Galimberti M, Clarke RJ, Pegoraro F, Ruhl H and Bulanov S (2002) Electric field detection in laser-plasma interaction experiments via the proton imaging technique. *Physics of Plasmas* **9**, 2214. doi:10.1063/1.1459457

7. Roth M, Cowan TE, Key MH, Hatchett SP, Brown C, Fountain W, Johnson J, Pennington DM, Snavely RA, Wilks SC, Yasuike K, Ruhl H, Pegoraro F, Bulanov SV, Campbell EM, Perry MD and Powell H (2001) Fast ignition by intense laser-accelerated proton beams. *Physical Review Letters* **86**, 436. doi:10.1103/PhysRevLett.86.436

8. Patel P, Mackinnon A, Key M, Cowan T, Foord M, Allen M, Price D, Ruhl H, Springer P and Stephens R (2003) Isochoric heating of solid-density matter with an ultrafast proton beam. *Physical Review Letters* **91**(12), doi:10.1103/PhysRevLett.91.125004

9. Esirkepov T, Borghesi M, Bulanov SV, Mourou G and Tajima T (2004) Highly efficient relativistic-ion generation in the laser-piston regime. *Physical Review Letters* **92**, 175003.

10. Henig A, Steinke S, Schnurer M, Sokollik T, Horlein H, Kiefer D, Jung D, Schreiber J, Hegelich BM, Yan XQ, Meyer-ter Vehn J, Tajima T, Nickles PV, Sandner W and Habs D (2009) Radiation-pressure acceleration of ion beams driven by circularly polarized laser pulses. *Physical Review Letters* **103**, 245003. doi:10.1103/PhysRevLett.103.245003

11. Kim IJ, Pae KH, Choi IW, Lee CL, Kim HT, Singhal H, Sung JH, Lee SK, Lee HW, Nickles PV, Jeong TM, Kim CM and Nam CH (2016) Radiation pressure acceleration of protons to 93 MeV with circularly polarized petawatt laser pulses. *Physics of Plasmas* **23**, 070701. doi:10.1063/1.4958654

12. Haberberger D, Tochitsky S, Fiuza F, Gong C, Fonseca RA, Silva LO, Mori WB and Joshi C (2011) Collisionless shocks in laser-produced plasma generate monoenergetic high-energy proton beams. *Nature Physics* **8**, 95. doi:10.1038/nphys2130

13. Pak A, Kerr S, Lemos N, Link A, Patel P, Albert F, Divol L, Pollock BB, Haberberger D, Froula D, Gauthier M, Glenzer SH, Longman A, Manzoor L, Fedosejevs R, Tochitsky S, Joshi C and Fiuza F (2018) Collisionless shock acceleration of narrow energy spread ion beams from mixed species plasmas using 1 μ m lasers. *Physical Review Accelerators and Beams* **21**, 103401. doi:10.1103/PhysRevAccelBeams.21.103401

14. Palmer CAJ, Dover NP, Pogorelsky I, Babzien M, Dudnikova GI, Ispiriyan M, Polyanskiy MN, Schreiber J, Shkolnikov P, Yakimenko V and Najmudin Z (2011) Monoenergetic proton beams accelerated by a radiation pressure driven shock. *Physical Review Letters* **106**, 14801. doi:10.1103/PhysRevLett.106.014801

15. Tresca O, Dover N, Cook N, Maharjan C, Polyanskiy M, Najmudin N, Shkolnikov P and Pogorelsky I (2015) Spectral modification of shock accelerated ions using a hydrodynamically shaped gas target. *Physical Review Letters* **115**, 094802. doi:10.1103/PhysRevLett.115.094802

16. Wei MS, Mangles SPD, Najmudin Z, Walton B, Gopal A, Tatarakis M, Dangor AE, Clark EL, Evans R, Fritzler S, Clarke RJ, Hernandez-Gomez C, Neely D, Mori W, Tzoufras M and Krushelnick K (2004) Ion acceleration by collisionless shocks in high-intensity-laser–underdense-plasma interaction. *Physical Review Letters* **93** 155003.

17. Fiuza F, Stockem A, Boella E, Fonseca RA, Silva LO, Haberberger D, Tochitsky S, Mori WB and Joshi C (2013) Ion acceleration from laser-driven electrostatic shocks. *Physics of Plasmas* **20**, 56304. doi:10.1063/1.4801526

18. Chen SN, Vranic M, Gangolf T, Boella E, Antici P, Bailly-Grandvaux M, Loiseau P, Pepin H, Revet G, Santos JJ, Schroer AM, Starodubstev M, Willi O, Silva LO, d'Humieres E and Fuchs J (2017) Collimated protons accelerated from an overdense gas jet irradiated by a 1 μm wavelength high-intensity short-pulse laser. *Scientific Reports* **7**, 13505. doi:10.1038/s41598-017-12910-6

19. Guerin S, Laval G, Mora P, Adam JC, Heron A and Bendib A (1995) Modulational and Raman instabilities in the relativistic regime. *Physics of Plasmas* **2**, 2807. doi:10.1063/1.871178

20. Kumar R, Sakawa Y, Sano T, Dohl LNK, Woolsey N and Morace A (2021) Ion acceleration at two collisionless shocks in a multicomponent plasma. *Physical Review E* **103**, 043201. doi:10.1103/PhysRevE.103.043201

21. Layer BD, York AG, Varma S, Chen YH and Milchberg HM (2009) Periodic index-modulated plasma waveguide. *Optics Express* **17**, 4263. doi:10.1364/oe.17.004263

22. Hagena OF (1981) Nucleation and growth of clusters in expanding nozzle flows. *Surface Science* **106**, 101. doi:10.1016/0039-6028(81)90187-4

23. Schindelin J, Rueden CT, Hiner MC and Eliceiri KW (2015) The ImageJ ecosystem: An open platform for biomedical image analysis. *Molecular Reproduction & Development* **82**, 518.

24. Willingale L, Mangles SPD, Nilson PM, Clarke RJ, Dangor AE, Kaluza MC, Karsch S, Lancaster KL, Mori WB, Najmudin Z, Schreiber J, Thomas AGR, Wei MS and Krushelnick K (2006) Collimated multi-MeV ion beams from high-intensity laser interactions with underdense plasma. *Physical Review Letters* **96**, 245002. doi:10.1103/PhysRevLett.96.245002

25. Penetrante BM, Wood WM, Siders CW, Bardsley JN and Downer MC, (1992) Ionization-induced frequency shifts in intense femtosecond laser pulses. *Journal of the Optical Society of America B* **9**, 2032. doi:10.1364/JOSAB.9.002032

26. Veisz L, Theobald W, Feurer T, Schwoerer H, Uschmann I, Renner O and Sauerbrey R (2004) Three-halves harmonic emission from femtosecond laser produced plasmas with steep density gradients. *Physics of Plasmas* **11**, 3311. doi:10.1063/1.1748174

27. Quesnel B, Mora P, Adam JC, Heron A and Laval G (1997) Electron parametric instabilities of ultraintense laser pulses propagating in plasmas of arbitrary density. *Physics of Plasmas* **4**, 3358. doi:10.1063/1.872494

28. Darrow CB, Coverdale C, Perry MD, Mori WB, Clayton C, Marsh K and Joshi C (1992) Strongly coupled stimulated Raman backscatter from subpicosecond laser-plasma interactions. *Physical Review Letters* **69**, 442. doi:10.1103/PhysRevLett.69.442

29. Fonseca RA, Silva LO, Tsung FS, Decyk VK, Lu W, Ren C, Mori WB, Deng S, Lee S, Katsouleas T and Adam JC (2002) OSIRIS: A three-dimensional, fully relativistic particle in cell code for modeling plasma based accelerators. In Sloot P, Hoekstra A, Tan CJ and Dongarra J (eds) *Computational Science—ICCS 2002: international Conference Amsterdam, The Netherlands, April 21–24, 2002 Proceedings, Part III 2*. Berlin, Heidelberg: Springer, 342–351.

30. Puyuelo-Valdes P, Henares JL, Hannachi F, Ceccotti T, Domange J, Ehret M, d'Humieres E, Lancia L, Marques JR, Ribeyre X, Santos JJ, Tikhonchuk V and Tarisien M (2019) Proton acceleration by collisionless shocks using a supersonic H2 gas-jet target and high-power infrared laser pulses. *Physics of Plasmas* **26**, 123109. doi:10.1063/1.5116337